IOP Publishing J. Phys. Photonics 2 (2020) 044001 https://doi.org/10.1088/2515-7647/aba670

Journal of Physics: Photonics

OPEN ACCESS

RECEIVED
6 May 2020

REVISED
30 June 2020

ACCEPTED FOR PUBLICATION
15 July 2020

PUBLISHED
12 August 2020

Original content from this work may be used under the terms of the Creative Commons Attribution 4.0 licence.

Any further distribution of this work must maintain attribution to the author(s) and the title of the work, journal citation and DOI.

PAPER

Spike-based information encoding in vertical cavity surface emitting lasers for neuromorphic photonic systems

Matěj Hejda, Joshua Robertson, Julián Bueno and Antonio Hurtado

Institute of Photonics, SUPA Department of Physics, University of Strathclyde, Glasgow, United Kingdom

E-mail: antonio.hurtado@strath.ac.uk

Keywords: neuromorphic photonics, vertical cavity surface emitting laser, optical neuron, spiking laser neuron, spike encoding

Abstract

The ongoing growth of use-cases for artificial neural networks (ANNs) fuels the search for new, tailor-made ANN-optimized hardware. Neuromorphic (brain-like) computers are among the proposed highly promising solutions, with optical neuromorphic realizations recently receiving increasing research interest. Among these, photonic neuronal models based on vertical cavity surface emitting lasers (VCSELs) stand out due to their favourable properties, fast operation and mature technology. In this work, we experimentally demonstrate different strategies to encode information into ultrafast spiking events in a VCSEL-neuron. We evaluate how the strength of the input perturbations (stimuli) influences the spike activation time, allowing for spike latency input coding. Based on a study of refractory behaviour in the system, we demonstrate the capability of the VCSEL-neuron to perform reliable binary-to-spike information coding with spiking rates surpassing 1 GHz. We also report experimentally on neuro-inspired spike firing rate-coding with a VCSEL-neuron, where the strength of the input perturbation (stimulus) is continuously encoded into the spiking frequency (spike firing rate). With the prospects of neuromorphic photonic systems constantly growing, we believe the reported functionalities with the ultrafast spiking VCSEL-neurons provide a reliable, multifaceted approach for interfacing photonic neuromorphic platforms with existing computation and communication systems.

1. Introduction

The advent of artificial neural networks (ANNs) marked a significant milestone in computer science, allowing computers to perform new complex tasks that typically require human reasoning, such as object recognition in images [1, 2] or natural language processing [3]. Nowadays, machine learning algorithms based on ANNs are quickly becoming ubiquitous, powering the services and systems we use in our daily lives [4–6]. However, conventional computers based on the von-Neumann architecture are not very well suited for ANNs due to their serial instruction processing and distinct memory and logic units. These facts, paired with the physical limits on further transistor size minimization (Dennard's scaling law [7]) and plateauing of Moore's law observed in recent years [8] have fuelled the search for new, 'beyond von-Neumann' computational architectures. The field of neuromorphic (brain-like) engineering aims at answering those needs by mimicking the functionality of biological brains and nervous systems in large-scale, densely interconnected networks of computing primitives (typically analog circuits or digital processors). These systems are characterised by propagating information using *spikes*: an asynchronous, sparse information encoding scheme observed in neurons that combines properties of both digital and analog signals. Whilst neuromorphic platforms such as Neurogrid [9] and Braindrop [10] from Stanford University, BrainScaleS [11] from Heidelberg University, Loihi [12] by Intel, SpiNNaker [13] from Manchester University and TrueNorth [14] by IBM have already demonstrated the viability and capabilities of brain-inspired hardware, there are certain limits imposed by their electronics-based character. Since one of the most fascinating characteristics of the brain is its remarkably low power consumption [15], neuromorphic systems are expected to enable highly energy-efficient functionality for future artificial intelligence applications. Given the fact that the processing performance in distributed systems significantly depends on the communication

© 2020 The Author(s). Published by IOP Publishing Ltd

efficiency between the nodes, the reliance of electronic neuromorphic systems on metallic interconnects leads to performance challenges and introduces bottlenecks due to radiative and RC physics [16]. While digital many-core systems (such as SpiNNaker) offer high degree of tunability for each node, making them suitable for simulations of neuronal networks in brains [17], the capability of analog systems to directly exhibit the dynamical behaviour similar to that observed in neurons, without the need to perform resource-intensive numerical simulation of it [18], further raises the prospects of these systems for high-speed, energy-efficient neuro-inspired computation.

Optical and photonic systems are a prime example of analog models with high prospects for computation, thanks to their intrinsic nonlinearities and use of optical waveguides that carry signals passively, with lower latency, higher possible bandwidth [19] and low electromagnetic interference. These systems can also operate at ultrafast operation rates with high power efficiency [20] and with additional degrees of freedom such as wavelength and polarization. There are a number of different approaches aiming towards the realization of ANNs using optics and photonics, including matrix-vector multiplicators [21] or arrays of cascaded optical modulators [22]. Neuromorphic photonic platforms represent a subset of these approaches with various photonic devices being investigated, with a non-exhaustive list of examples including optical modulators [23, 24], phase change materials [25–27], resonant tunnelling diode-laser diode coupled systems [28–30], quantum-dot lasers [31, 32], silicon photonic components and circuits [33–35], micropillar lasers [36, 37] and superconducting optoelectronic circuits [38, 39].

Among the most promising neuromorphic photonics technologies are vertical cavity surface emitting lasers (VCSELs). Thanks to their viability for large-scale, high throughput fabrication, these compact devices are inexpensive and readily commercially available. They can operate at standard telecom wavelengths, have low lasing thresholds and exhibit rich nonlinear dynamics [40]. For example, when subject to different types of polarised optical injection, VCSELs can show bistability, polarization switching [41, 42] and a wide range of complex nonlinear responses, ranging from periodical dynamics to chaos and excitable responses [43, 44]. Therefore, the use of these devices as artificial photonic spiking neurons has been proposed in recent years [45, 46]. Specifically, controlled excitation [47], inhibition [48] and propagation [49] of neuron-like spiking regimes have been demonstrated in VCSELs at operation rates up to seven orders of magnitude higher than the timescales of biological neurons. These functionalities can be used to demonstrate toy models of optical [50] and auditory [51] pathways or for supervised pattern recognition [52, 53].

While the mystery of biological neural coding has not yet been fully uncovered, multiple different ways of stimuli representation have been observed in neural codes [54]. In general, information communicated between neurons can be encoded using either rate-coding of spike trains (number of spikes in a given time window) or precise spike timing (temporal coding), with spike timing precision (at the ms timescales) being crucial for information encoding and processing in biological neural systems [55]. Hence, an implementation that delivers reliable, digital-to-spike conversion at high data rates is essential to facilitate brain-inspired information encoding and bridge future neuromorphic computing platforms with conventional digital computers and telecommunication networks [56]. Previous numerical studies have reported a wide range of spike encoding capabilities in neuromorphic photonic systems. Both precise spike timing and rate coding regimes were observed in a single section quantum-dot InAs/GaAs laser model [63]. In the VCSEL-SA based models, sound azimuth information was encoded in the interval between two spikes [51] and rate-coded trains were elicited from a single laser [64] as well as propagated between two mutually coupled devices [65].

In this work, we demonstrate the viability of photonic spiking VCSEL-neuron for high-speed, spike-based information encoding in the optical domain. The information injected to the neuron is encoded either using a binary-to-spike encoding scheme for digital signals, or biologically inspired intensity-to-firing rate encoding scheme for continuous signals. Both absolute and relative refractoriness in the neuron are evaluated and used to estimate the maximum operation frequency of the neuron in the binary-to-spike regime. The dependence of spike activation time as a function of input perturbation strength is also investigated, with prospects for latency-based information encoding. Moreover, these experiments are realized using a commercially available VCSEL operating at a standard telecom wavelength of 1310 nm, which makes our approach fully compatible with current optical telecommunication networks.

2. Methods

Simplified schematics of our proposed VCSEL-based photonic spiking neuron and the two optical approaches for high-speed temporal spike encoding and intensity-to-firing rate encoding are provided in figures 1(a) and (b), respectively. All the experiments carried out in this work have been realized using the experimental setup shown in figure 2(a). The optical spiking neuron is implemented using an off-the-shelf fibre-coupled 1310 nm VCSEL (RayCan) mounted in a thermoelectrically cooled laser diode mount. The laser is temperature stabilized (Thorlabs TED200C) at the temperature of 298 K and biased with a current

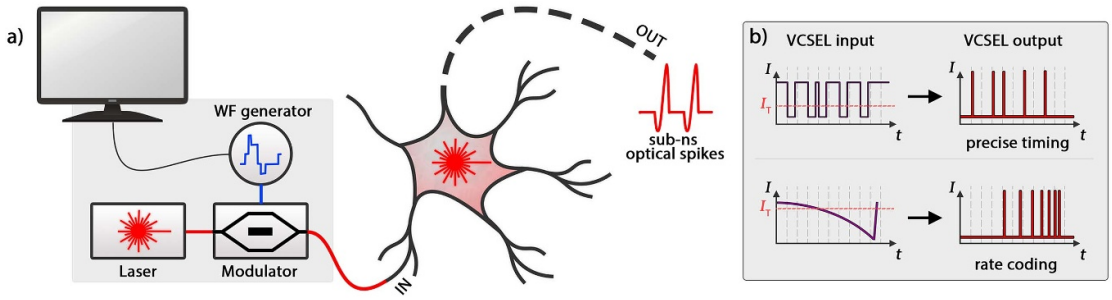

Figure 1. (a) Schematic of the system used to obtain sub-ns optical spiking responses from a photonic spiking VCSEL-neuron. (b) Diagram of the two main operational modes investigated: precise spike timing and rate-coding regimes.

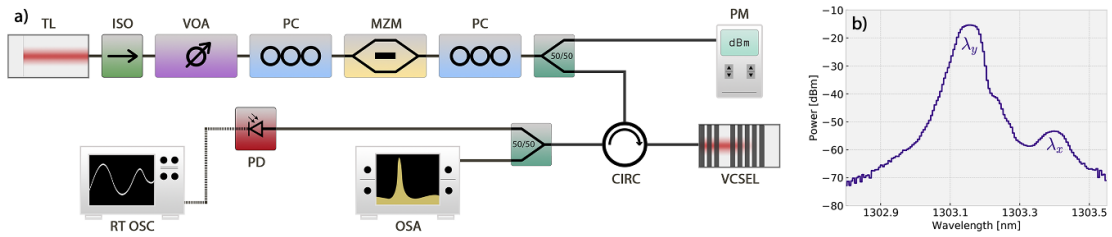

Figure 2. (a) Diagram of the experimental setup. TL—tunable laser; ISO—optical isolator; VOA—variable optical attenuator; PC—polarization controller; 50/50—optical splitter; PM—optical power meter; CIRC—optical circulator; OSA—optical spectrum analyzer; PD—photodetector; RT OSC—real-time oscilloscope. (b) Optical spectrum of the solitary VCSEL used in this study at $I = 5$ mA and $T = 298$ K. The VCSEL's two polarization modes are referred to as λ_y (parallel) and λ_x (orthogonal).

well above the device's lasing threshold ($I = 5$ mA, $I_{thr} = 1.65$ mA). The spectrum of the laser, shown for $I = 5$ mA at 298 K in figure 2(b), exhibits two peaks that correspond to the two orthogonal polarizations of the fundamental transverse mode of the device. These are referred to as parallel (the dominant peak, denoted λ_y) and orthogonal (the secondary peak, denoted λ_x) polarized modes.

The photonic neuron operation relies on coherent injection locking of the VCSEL to a signal from an external tunable laser source (TL; Santec TSL210V). The information input to the system is realized by modulating the intensity of TL's light using a Mach–Zehnder modulator (MZM), which is controlled by RF signals from an arbitrary waveform generator (AWG) (Keysight, M8190A) operating at 12 GSa s^{-1}. These RF signals were amplified using a 10 dBm amplifier (Mini-Circuits, ZX60-14012l-S+) before entering the MZM. First, the TL signal is passed through an optical isolator to ensure unidirectional coupling between the lasers. Following that, the power is adjusted using a variable optical attenuator and the signal is polarization matched to the MZM using a polarization controller. The modulator bias point is set to achieve maximal average power while preserving full modulation amplitude (modulations are typically rectangular-shaped drops, see figure 1(b)). The modulated signal is polarization matched to the orthogonally polarised mode of the VCSEL, before its injection into the device through a 50:50 coupler and an optical circulator. The other branch of this coupler is used to record the average injection power P_{inj} using a power meter (PM). The TL wavelength is matched to the selected peak in the laser spectra with a certain frequency detuning Δ_f. The detuning and injection power are the main operational parameters defining the distance of the unlocking boundary (threshold) from the locked (steady) state. In this steady (non-spiking) state, the VCSEL-neuron is fully locked to the TL. By bringing the system close to the unlocking boundary and modulating the amplitude of the injection signal, the VCSEL-neuron responds with well controlled, very fast (sub-nanosecond) optical spiking responses [47]. In general, higher detuning and lower injection power bring the threshold closer to the steady state. With a high injection power, locking can be achieved more easily, but large drops may be needed to activate spikes. Larger drops also facilitate faster continuous spiking (rate coding). The detuning and power values used through this work were found experimentally based on values used in previous works (see [66]). The laser output passes again through the circulator into a 50:50 coupler for analysis in an optical spectrum analyser and a real-time oscilloscope (RT OSC). In the oscilloscope line, the optical signal is converted to the electrical domain using a high-speed fibre-coupled amplified photodetector (PD; Thorlabs PDA8GS). The signal being injected into the VCSEL-neuron is recorded using the PD and RT OSC from the PM branch. The setup is fully realized using commercial fibre optic components at standard telecom wavelengths.

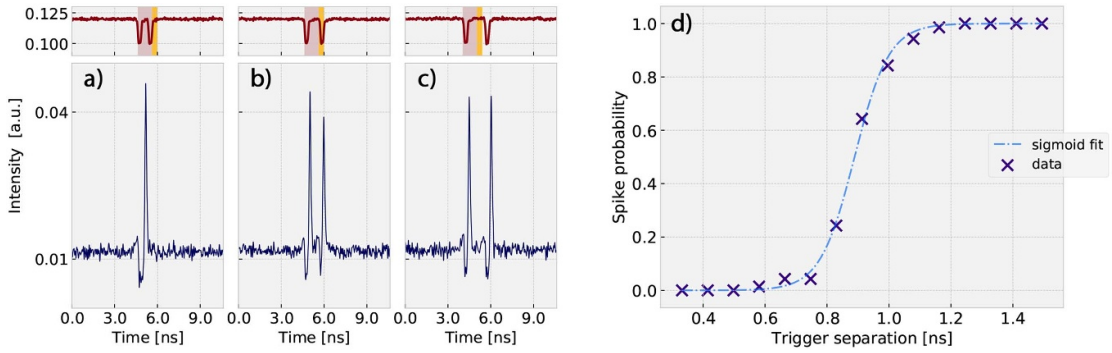

Figure 3. Refractory period of the VCSEL-neuron for $P_{inj} = 160\ \mu$W and $\Delta_f = -6.7$ GHz. (a)–(c) The time-traces in the upper row (red) show pairs of perturbations with increasing temporal separation injected into the VCSEL-neuron. (a) When the second perturbation arrives within the absolute refractory period (highlighted in red shading), only first spike is elicited from the VCSEL-neuron (bottom row, blue). For (b), where perturbations have temporal separation larger than the absolute refractory period, but lower than the relative refractory period (highlighted in orange shading), a second spike is elicited with certain probability. Temporal distances between the injected pulses are (a) 0.75 ns, (b) 1.08 and (c) 1.49 ns. (d) Probability of the firing of a second spike versus temporal separation between perturbations. Results are calculated from 70 consecutive measurement cycles and a sigmoid function fit is shown for comparison. There is a clear transition between absolute (no spiking observed) and relative refractory period (reduced spiking probability) followed by recovered state (spiking probability very close to unity).

The modulation schemes are depicted in figure 1(b). For the investigation of the refractory behaviour and the binary-to-spike format conversion in VCSEL-neurons, the modulation entails short rectangular-shaped intensity drops, where each drop serves to elicit one single spike during its duration. The amplitude of the drops can be variable or fixed (binary modulation). Only drops with sufficient amplitude cross the spiking threshold (depicted as red dashed line I_T in figure 1(b)) and elicit the spikes. In the rate-coding demonstration of the VCSEL-neuron, an arbitrary continuous signal is used for intensity modulation. The information is encoded into the signal's intensity, such that 'stronger' stimuli correspond to larger drops in injection power. The modulation signal must cross a certain threshold level to trigger continuous spiking responses.

3. Results and discussion

Multiple injection modulation schemes were used to demonstrate the different properties and responses of the VCSEL-neuron investigated in this work. In figures 3–6, upper (red) time-traces denote the intensity of the modulated signal from the TL injected into the VCSEL-neuron, whilst lower (blue) time-traces correspond to the response of the VCSEL.

3.1. Refractoriness of the VCSEL-neuron

To evaluate the refractory period of the VCSEL-neuron, multiple pairs of rectangular-shaped intensity perturbations (0.249 ns wide), with varying temporal separation between them (figure 3), were used as the input modulated signals, The separation Δt, measured between the two input pulse rising edges, was gradually increased from 0.332 ns to 1.494 ns, in steps of 83 ps. The first recorded perturbation arrives when the VCSEL-neuron is in a locked (resting) state and always triggers a spiking response at the device's output. When the second perturbation arrives too soon after the first one (figure 3(a)), the system is still inside the so-called *absolute refractory period* ($\Delta t < \tau_{abs}$) and cannot elicit another spiking response. However, when stimuli separation time reaches the edge of the absolute refractory period (~0.83 ns, figure 3(b)), occurrences of second spikes can be observed, with probability of second spike increasing as Δt is increased further from τ_{abs}. The absolute refractory period is highlighted as a red shaded area in figures 3(a)–(c). Simultaneously, it was observed that the amplitude of the second spike was slightly lower for spikes very close to τ_{abs}, further increasing with larger Δt. The relative number of observed second spiking events for the same dataset is depicted in figure 3(d) as a function of trigger pulse separation. The blue dash-dotted line shows a sigmoid curve fit to the calculated spike probability. For Δt above 1.08 ns, figure 3(d) shows the probability of second spiking event reaching near certainty. After this time period (denoted as *relative refractory period* τ_{rel}, highlighted in orange shading in figures 3(a)–(c)), the dynamical system is sufficiently recovered and capable of properly responding with another spike. Hence, to ensure highly reliable activation of spikes with precise timing, the VCSEL-neuron should be operated with minimal inter-spike temporal separation equal or larger to the relative refractory period.

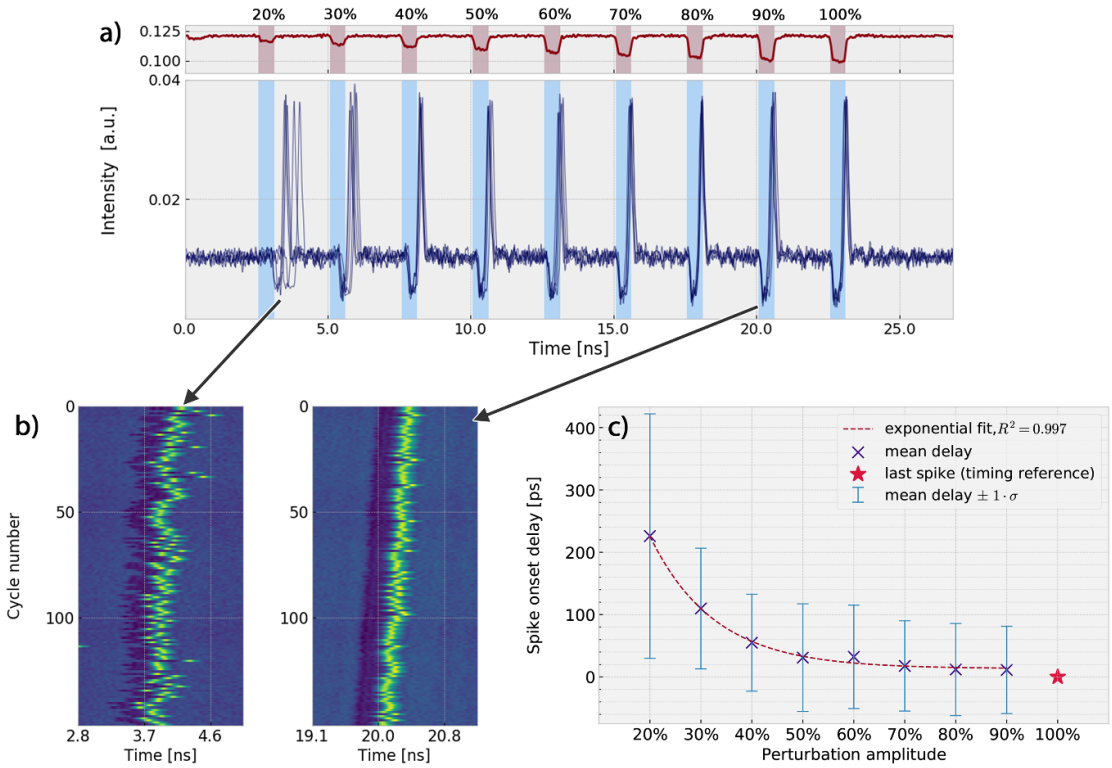

Figure 4. (a) Spiking responses of the VCSEL-neuron ($P_{inj} = 162\ \mu$W, $\Delta_f = -7.2$ GHz) as a function of perturbation amplitude showing different spike latency and jitter behaviour. The superposition of five responses (blue) to consecutive and identical input perturbation patterns (red) are shown. Low amplitude perturbations result in a spike activation delay and higher onset irregularity. (b) Temporal maps of 150 measurement cycles of VCSEL-neuron, showing responses to 20% (left) and 90% (right) strength perturbations. There is pronounced jittering across the cycles for low-amplitude perturbations. (c) Results of spike onset delay time as a function of perturbation strength (percentage of available DAC range), calculated for 150 cycles. The last spike (triggered by perturbation with 100% amplitude) is used as timing reference between the measurement cycles.

3.2. Spike latency in VCSEL-neurons for stimulus strength encoding

The perturbation intensity of the injected signals (stimuli) also influences the spiking response in the VCSEL-neuron. To analyse this phenomenon, we devised an experiment where we inject stimuli into the VCSEL-neuron with different controlled intensities and analyse the temporal features of the triggered spiking responses. To do this, the available amplitude range of the digital-to-analog converter (DAC) on the AWG was divided into ten equidistant levels. These were used to create a modulation waveform of ten rectangular-shaped drops of varying intensity, each with a temporal length of 0.5 ns and separated by 2 ns.

Figure 4(a) shows the response of the VCSEL-neuron to gradually increasing perturbations (with 20%–100% of DAC amplitude range). The bottom plot in figure 4(a) shows (in blue) five superimposed time-series captured at the output of the VCSEL-neuron in response to five identical input perturbation patterns (shown in red in figure 4(a)). These patterns were injected into the device in consecutive measurements. All the injected perturbations successfully pushed the VCSEL-neuron through its spiking threshold, triggering the firing of a single spike. For the low-amplitude (leftmost) perturbations shown in figure 4(a), the spiking response exhibits both a pronounced onset delay and jittering. More information regarding the responses across multiple consecutive measurements can be seen in the temporal maps in figure 4(b) for two selected perturbation depths (20% and 90%). These maps show the spikes generated at the VCSEL-neuron's output when an identical input perturbation enters the laser 150 times. Green colour represents high output signal amplitude (spike crests) while blue represents low-amplitude (background, no activity). The maps further confirm that both the low and high amplitude input signals resulted in spiking responses in all the cycles. The spikes triggered by the low-amplitude perturbation exhibit increased temporal jittering. This effect vanishes when perturbations with larger amplitude are used. Figure 4(c) shows the average spike activation delay for each of the stimuli strengths, calculated from 150 measurement cycles. The last spike was used as a timing reference between measurement cycles, hence its delay is fixed to zero. For very low-amplitude stimuli, there is a significant increase in mean spike onset delay as well as the standard deviation (due to the jittering). The high R^2-fit suggests that for linearly increasing perturbation strength, the mean spike activation time in the VCSEL-neuron decays exponentially and later stabilizes near a certain fixed value.

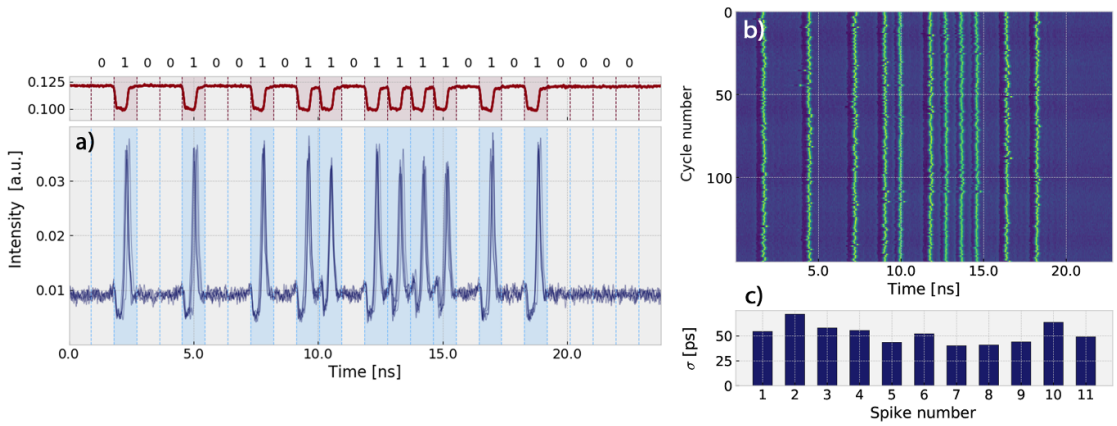

Figure 5. Binary-to-spiking information encoding for return-to-zero input code at 1.09 GHz with a VCSEL-neuron ($P_{inj} = 178\ \mu$W, $\Delta_f = -6.7$ GHz). (a) The encoded information, a sequence of 24 bits, is shown (in red) in the top row. The bottom plot shows the superposition of five time-series recorded at the output of the VCSEL-neuron for identical injection patterns. (b) Temporal map showing the response of the VCSEL-neuron to 150 consecutive cycles of the same digital 'IoP' input pattern. (c) Standard deviation of timing for each spike, measured across the 150 repetition cycles shown in the temporal map.

It is worth noting that all recorded spiking responses in this experiment had the same amplitude. The results shown on figure 4(b) suggest that the larger drop amplitudes result in improved control over the spike activation process, both in terms of stable onset delay and reduced temporal jittering. Furthermore, these observations hint towards the capability of the VCSEL-neuron to encode stimuli information into spike latency coding, an encoding approach observed, among others, in retinal ganglion cells [57]. This approach will be further investigated in following studies.

3.3. Information encoding with precise spike timing in a VCSEL-neuron

By injecting controlled intensity perturbations into the VCSEL-neuron with: (a) temporal separation higher than the system's relative refractory period, and (b) sufficiently high amplitude beyond the excitation threshold, spike trains with precise timing can be obtained with high reliability and low temporal jitter. We utilize this capability of the VCSEL-neuron to demonstrate its function for information encoding of digital binary signals into spike train representation in the optical domain. Figure 5(a) plots the time-series captured at the output of the VCSEL-neuron under the injection of a binary ASCII representation of the word 'IoP', an acronym of the Institute of Photonics at the University of Strathclyde. Figure 5(a) shows an overlay of five consecutive responses from the VCSEL-neuron to the injection of the 'IoP' pattern, clearly revealing that the binary digital information is encoded into a spike train generated by the VCSEL-neuron. The binary representation is shown as series of ones and zeros at the top of the figure. The injection signal is modulated using unipolar, return-to-zero (RZ) serial encoding scheme. Since spikes in the VCSEL-neuron are elicited by short optical power drops, the Mach–Zehnder modulator is biased in such an operating point that the polarity of the modulation RZ waveform is inverted, with zero level now set at higher power level. In accordance with results shown in previous section, any injection intensity drop that overcomes the threshold (see figure 1(b)) causes spiking. In order to obtain reliable, low latency spikes for each bit, full range of the AWG DAC was used, resulting in approx. 18% power drops in the injection signal ($K_p = 0.18$, see [67] for more details). The temporal length of one bit is 0.916 ns, with 54.5% duty cycle. This corresponds to a bit rate of 1.09 Gbps. For a '1′ input bit, a single spike is excited at the VCSEL-neuron's output, whilst for a '0′ input bit, the VCSEL-neuron remains quiescent as it is in its injection locked (steady) state. In agreement with [58], it was observed that the duration of the incoming perturbations (input bits in this case) does not have an effect on the response as long as it remains shorter than the absolute refractory period of the device. The temporal stability map shown in figure 5(b) depicts in a single plot 150 consecutive responses (cycles) of the VCSEL-neuron to the same input 'IoP' digital pattern, clearly illustrating the reproducibility of the proposed digital-to-spiking encoding mechanism. Good spike timing consistency is further confirmed by the means of standard deviation of activation times, shown in figure 5(c). By operating at 0.916 ns bit^{-1}, the VCSEL-neuron facilitates binary-to-spike conversion rate of 1.09 Gbps, over four times higher than the values 0.27 Gbps theoretically predicted on other photonic neuronal models [59]. It is worth noting that the phrase length (24 bits) was selected for proof-of-concept due to its easy visualization. In principle, there are no limits imposed by the VCSEL-neuron in terms of encoded phrase length.

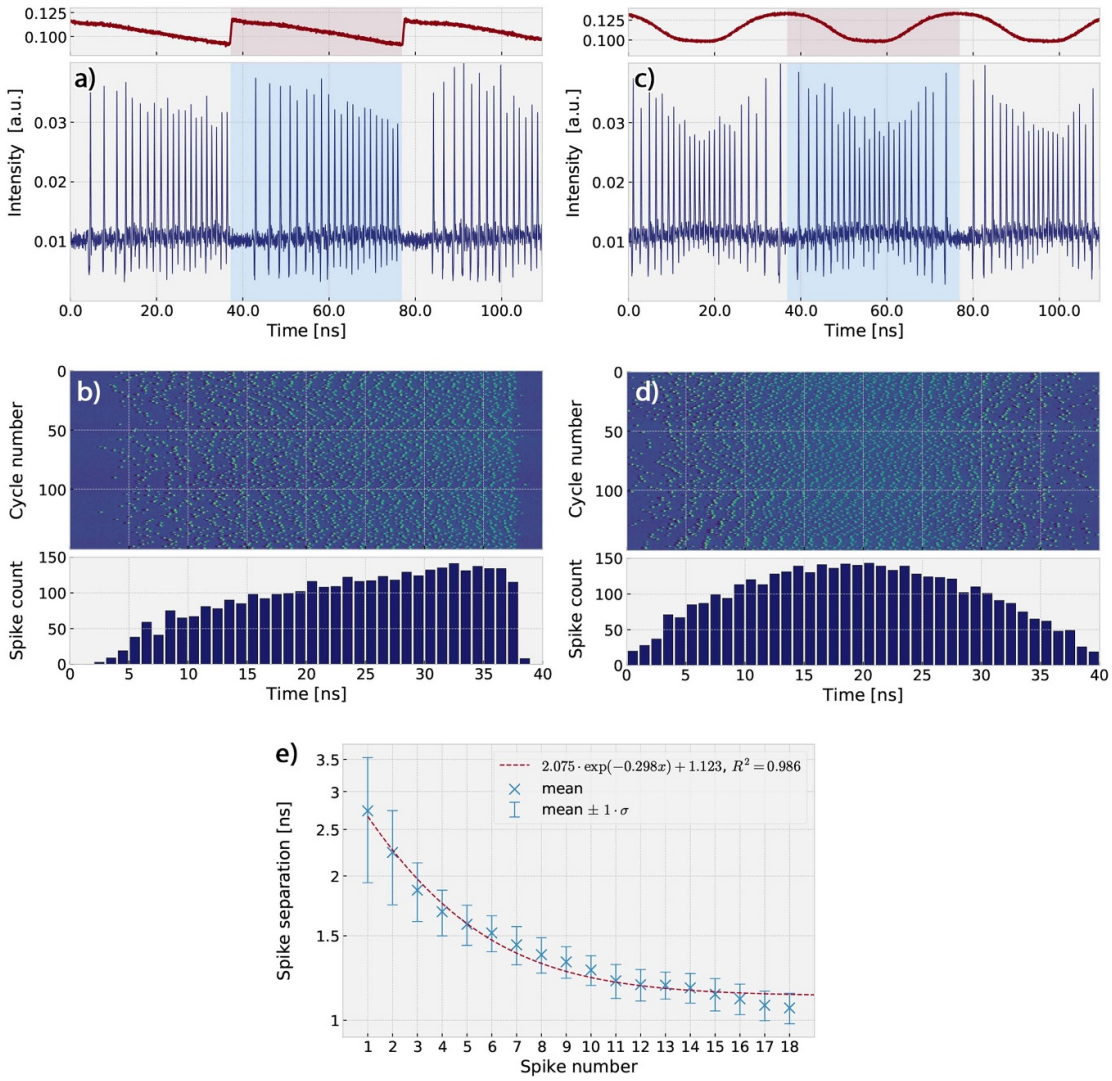

Figure 6. (a) Spike rate-coding in a VCSEL-neuron with a sawtooth wave modulation ($P_{inj} = 143$ μW, $\Delta_f = -6.3$ GHz). As the amplitude decreases further from the steady state, the spiking rate increases. When the device returns to the initial steady state, spiking is inhibited until the modulation signal causes another transition to the spiking dynamical region. A period of the signal (highlighted in blue shading) is visualized in the temporal map (b) for 150 repetitions, with histogram showing number of observed spikes per 1 ns long bin across the 150 shown cycles; (c) Spike rate-coding with a sine wave (non-monotonous) modulation ($P_{inj} = 134$ μW, $\Delta_f = -6.3$ GHz). (d) Temporal map (150 repetitions) for the blue highlighted sine modulation period, with histogram showing number of observed spikes per 1 ns long bin across the 150 shown cycles. (e) Average temporal separation of the first 18 spikes (calculated from nth to $(n+1)$th spike), obtained from 135 measurement cycles of the sawtooth modulation. The averages were fitted with exponential curve (red dotted line).

3.4. Information encoding with spike firing rate-coding

The functionality of the VCSEL-neuron is not only limited to digital input operation. Figure 6 demonstrates the capability of the VCSEL-neuron to encode the intensity of varying amplitude stimuli into its spike firing frequency. In biological neurons, this behaviour is referred to as *Class 1 neural excitability* and it can be observed for example in cortical excitatory pyramidal neurons [60]. Unlike classical analog-to-digital converters, which convert continuous-time signals into discrete-time, binary-coded forms, the VCSEL-neuron converts the signal magnitude into a spike firing rate, effectively realizing analog-to-spike rate-coding directly in the optical domain. Figures 6(a) and (b) plot results measured at the VCSEL-neuron's output under the injection of a sawtooth-shaped input signal with a repetition frequency of $f = 25$ MHz. As the intensity of the injected signal decreases, it crosses the activation threshold of the VCSEL-neuron, resulting in the firing of spikes at its output. These are initially triggered at a low spike firing rate, which rapidly grows as the input intensity decreases. A similar behaviour can be observed under the injection of a sinusoidal input signal with a frequency of $f = 25$ MHz, as seen in figures 6(c) and (d). In the second case, it is clearly observable how the spike firing rate periodically increases and decreases in response to the input intensity-modulated signal. To the best of our knowledge, this is the first demonstration of spike rate-coding as a function of input stimuli intensity in a photonic neuron. The temporal maps and histograms in figures

6(b) and (d) merge in a single plot the response of the VCSEL-neuron to 150 consecutive input triangle and sinusoidal input signals. For better clarity, a single response (or cycle) is highlighted in colour shaded areas in figures 6(a) and (c). For both sawtooth (periodically monotonous) and sinusoidal (non-monotonous) cases of injected analogic signals, consistent behaviour can be observed in the output patterns. Simultaneously, a clear relationship between the amplitude of the input signal and the observed spiking frequency at the output of the VCSEL-neuron is seen. As the modulation strength increases in time, the density (frequency) of spikes increases across all the recorded cycles. Unlike in the precise spike timing case (see figure 5), there is now higher randomness in the timing of the first spike between the cycles. This can be attributed to small noise variations in system conditions between the subsequent measurements, which cause the laser to cross the spiking boundary at slightly different time among different cycles. However, since the information in the rate-coding approach is represented in the frequency and not the spike time itself, we believe this behaviour is not detrimental to the reported functionality. Once the system crosses the spiking regime boundary, the timing of subsequent spikes among the cycles exhibits good level of consistency. It is also worth noting that in situations where the second spike is elicited within the relative refractory period (like continuous spiking at high frequencies), a slight decrease in the output spike amplitude can be observed. Since this amplitude suppression effect is also observed in biological neuronal models, we believe this is not detrimental to the computational capability of a system that would rely on rate-coded VCSEL-neurons. The effect of reduced spike amplitude during excitation in the relative refractory period was reported in the classical Hodgkin & Huxley dynamical model of squid axons [68]. Based on this effect, these neuronal models exhibit spike amplitude attenuation in their elicited spike trains during high-rate continuous spiking [69].

Figure 6(e) shows the measured average inter-spike temporal separation for the case of the sawtooth wave modulation, measured across 135 cycle repetitions. The average is calculated for the first 18 spikes in each cycle, with an exponential line of best fit shown as dashed red line. For this case of approximately linearly increasing modulation strength, the inter-spike temporal spacing follows an exponential decay, until it reaches minimal values close to the absolute refractory period of the system. The exponential relation between observed spiking frequency and function of stimuli strength is in agreement with behaviour observed in Class 1 neurons [61] modelled using the Wilson–Cowan model [62], further confirming the similarity between the dynamical behaviour of our VCSEL-neuron and biological neurons.

4. Conclusions

We demonstrate experimentally the information encoding capabilities of a spiking photonic neuron running at ultrafast rates, based on an off-the-shelf VCSEL operating at telecom wavelengths. First, we experimentally investigate the refractory behaviour of the VCSEL-neuron and observe both absolute and relative refractory periods of $\sim$ 0.8ns and $\sim$ 1.1ns respectively. We also demonstrate and evaluate how the amplitude of the input stimulus influences the spike onset timing, permitting the use of spike latency to encode the intensity information of incoming stimuli. Based on the refractory period findings, we demonstrate experimentally the capability of the VCSEL-neuron to perform all-optical spike information encoding. Two different ways of signal encoding into spikes are introduced. First, we demonstrate precise spike timing encoding, where we utilize standard RZ serial encoding scheme for conversion of a 24-bit binary sequence into an optical spike train at rates over 1 Gbps. This bit sequence was selected as a representation of the three-letter word 'IoP' (acronym of Strathclyde's Institute of Photonics) in ASCII, but the same VCSEL-neuron is also capable of encoding arbitrarily long bit sequences. Secondly, we demonstrate biologically inspired rate-coding for periodically monotonous and non-monotonous input signals, where the strength (amplitude) of input optical stimuli is translated into the firing rate of the VCSEL-neuron. Both the temporal and rate-coding of spike trains have been observed in biological neurons, and as such, a device enabling reliable encoding using both of these information representation schemes at very high speeds (GHz rates) will be crucial for interfacing future photonic neuromorphic systems with both digital and analog inputs from devices such as sensors as well as additional (optical) processing and communication systems.

Acknowledgments

The authors acknowledge funding support by the European Commission (Grant 828841-ChipAI-H2020-FETOPEN-2018–2020), the Office of Naval Research Global (Grant ONRGNICOPN62909-18-1-2027) and the UK Engineering and Physical Sciences Research Council Doctoral Training Partnership (EP/N509760). We thank Prof T Ackemann and Prof A Kemp (University of Strathclyde) for lending some of the equipment used in this work.

ORCID iDs

Matěj Hejda https://orcid.org/0000-0003-4493-9426
Joshua Robertson https://orcid.org/0000-0001-6316-5265
Antonio Hurtado https://orcid.org/0000-0002-4448-9034

References

[1] He K, Zhang X, Ren S and Sun J 2016 Deep residual learning for image recognition *2016 IEEE Conf. on Computer Vision and Pattern Recognition (CVPR)* (IEEE) pp 770–8
[2] Zhao Z-Q, Zheng P, Xu S-T and Wu X 2019 Object detection with deep learning: a review *IEEE Trans. Neural Networks Learn. Syst.* **30** 3212–32
[3] Devlin J, Chang M-W, Lee K and Toutanova K 2018. BERT: pre-training of deep bidirectional transformers for language understanding arXiv:1810.04805
[4] Chen C, Zhang J, Xie Y, Xiang Y, Zhou W, Hassan M M, AlElaiwi A and Alrubaian M 2015 A performance evaluation of machine learning-based streaming spam tweets detection *IEEE Trans. Comput. Social Syst.* **2** 65–76
[5] Wright J, Yang A Y, Ganesh A, Sastry S S and Yi M 2009 Robust face recognition via sparse representation *IEEE Trans. Pattern Anal. Mach. Intell.* **31** 210–27
[6] Redmon J, Divvala S, Girshick R and Farhadi A 2016. You only look once: unified, real-time object detection *2016 IEEE Conf. on Computer Vision and Pattern Recognition (CVPR)* (IEEE) pp 779–88
[7] Dennard R H, Gaensslen F H, Yu H-N, Rideout V L, Bassous E and LeBlanc A R 1974 Design of ion-implanted MOSFET's with very small physical dimensions *IEEE J. Solid-State Circuits* **9** 256–68
[8] Peper F 2017 The end of Moore's law: opportunities for natural computing? *New Gener. Comput.* **35** 253–69
[9] Benjamin B V, Gao P, McQuinn E, Choudhary S, Chandrasekaran A R, Bussat J-M, Alvarez-Icaza R, Arthur J V, Merolla P A and Boahen K 2014 Neurogrid: a mixed-analog-digital multichip system for large-scale neural simulations *Proc. IEEE* **102** 699–716
[10] Neckar A, Fok S, Benjamin B V, Stewart T C, Oza N N, Voelker A R, Eliasmith C, Manohar R and Boahen K 2019 Braindrop: a mixed-signal neuromorphic architecture with a dynamical systems-based programming model *Proc. IEEE* **107** 144–64
[11] Friedmann S, Schemmel J, Grubl A, Hartel A, Hock M and Meier K 2017 Demonstrating hybrid learning in a flexible neuromorphic hardware system *IEEE Trans. Biomed. Circuits Syst.* **11** 128–42
[12] Davies M *et al* 2018 Loihi: a neuromorphic manycore processor with on-chip learning *IEEE Micro* **38** 82–99
[13] Painkras E, Plana L A, Garside J, Temple S, Galluppi F, Patterson C, Lester D R, Brown A D and Furber S B 2013 SpiNNaker: A 1-W 18-core system-on-chip for massively-parallel neural network Simulation *IEEE J. Solid-State Circuits* **48** 1943–53
[14] DeBole M V *et al* 2019 TrueNorth: accelerating from zero to 64 million neurons in 10 years *Computer* **52** 20–29
[15] Sengupta B and Stemmler M B 2014 Power consumption during neuronal computation *Proc. IEEE* **102** 738–50
[16] Nahmias M A, Tait A N, Shastri B J, de Lima T F and Prucnal P R 2015 Excitable laser processing network node in hybrid silicon: analysis and simulation *Opt. Express* **23** 26800
[17] Rhodes O, Peres L, Rowley A G D, Gait A, Plana L A, Brenninkmeijer C and Furber S B 2020 Real-time cortical simulation on neuromorphic hardware *Phil. Trans. R. Soc.* A **378** 20190160
[18] Indiveri G *et al* 2011 Neuromorphic silicon neuron circuits *Front. Neurosci.* **5** 73
[19] Ferreira de Lima T, Shastri B J, Tait A N, Nahmias M A and Prucnal P R 2017 Progress in neuromorphic photonics *Nanophotonics* **6** 577–99
[20] Miller D A B 2017 Attojoule optoelectronics for low-energy information processing and communications *J. Light. Technol.* **35** 346–96
[21] Hamerly R, Bernstein L, Sludds A, Soljačić M and Englund D 2019 Large-scale optical neural networks based on photoelectric multiplication *Phys. Rev.* X **9** 021032
[22] Shen Y *et al* 2017 Deep learning with coherent nanophotonic circuits *Nat. Photonics* **11** 441
[23] George J K, Mehrabian A, Amin R, Meng J, de Lima T F, Tait A N, Shastri B J, El-Ghazawi T, Prucnal P R and Sorger V J 2019 Neuromorphic photonics with electro-absorption modulators *Opt. Express* **27** 5181
[24] Ferreira de Lima T, Tait A N, Saeidi H, Nahmias M A, Peng H, Abbaslou S, Shastri B J and Prucnal P R 2019 Noise analysis of photonic modulator neurons *IEEE J. Selected Topics Quantum Electron.* **26** 1–8
[25] Feldmann J, Youngblood N, Wright C D, Bhaskaran H and Pernice W H P 2019 All-optical spiking neurosynaptic networks with self-learning capabilities *Nature* **569** 208–14
[26] Carrillo S G-C, Gemo E, Li X, Youngblood N, Katumba A, Bienstman P, Pernice W, Bhaskaran H and Wright C D 2019 Behavioral modeling of integrated phase-change photonic devices for neuromorphic computing applications *APL Mater.* **7** 091113
[27] Chakraborty I, Saha G, Sengupta A and Roy K 2018 Toward fast neural computing using all-photonic phase change spiking neurons *Sci. Rep.* **8** 12980
[28] Romeira B, Javaloyes J, Ironside C N, Figueiredo J M L, Balle S and Piro O 2013 Excitability and optical pulse generation in semiconductor lasers driven by resonant tunneling diode photo-detectors *Opt. Express* **21** 20931
[29] Romeira B, Avó R, Figueiredo J M L, Barland S and Javaloyes J 2016 Regenerative memory in time-delayed neuromorphic photonic resonators *Sci. Rep.* **6** 19510
[30] Romeira B, Figueiredo J M L and Javaloyes J 2017 Delay dynamics of neuromorphic optoelectronic nanoscale resonators: perspectives and applications *Chaos* **27** 114323
[31] Mesaritakis C, Kapsalis A, Bogris A and Syvridis D 2016 Artificial neuron based on integrated semiconductor quantum dot mode-locked lasers *Sci. Rep.* **6** 39317
[32] Robertson J, Ackemann T, Lester L F and Hurtado A 2018 Externally-triggered activation and inhibition of optical pulsating regimes in quantum-dot mode-locked lasers *Sci. Rep.* **8** 12515
[33] Van Vaerenbergh T, Fiers M, Dambre J and Bienstman P 2012 Simplified description of self-pulsation and excitability by thermal and free-carrier effects in semiconductor microcavities *Phys. Rev.* A **86** 063808
[34] Tait A N, Ferreira de Lima T, Zhou E, Wu A X, Nahmias M A, Shastri B J and Prucnal P R 2017 Neuromorphic photonic networks using silicon photonic weight banks *Sci. Rep.* **7** 7430
[35] Katumba A, Freiberger M, Laporte F, Lugnan A, Sackesyn S, Ma C, Dambre J and Bienstman P 2018 Neuromorphic computing based on silicon photonics and reservoir computing *IEEE J. Sel. Top. Quantum Electron.* **24** 1–10

[36] Selmi F, Braive R, Beaudoin G, Sagnes I, Kuszelewicz R, Erneux T and Barbay S 2016 Spike latency and response properties of an excitable micropillar laser *Phys. Rev.* E **94** 042219
[37] Pammi V A, Alfaro-Bittner K, Clerc M G and Barbay S 2020 Photonic computing with single and coupled spiking micropillar lasers *IEEE J. Sel. Top. Quantum Electron.* **26** 1–7
[38] Shainline J M, Buckley S M, Mirin R P and Nam S W 2017 Superconducting optoelectronic circuits for neuromorphic computing *Phys. Rev. Appl.* **7** 034013
[39] Shainline J M 2020 Fluxonic processing of photonic synapse events *IEEE J. Sel. Top. Quantum Electron.* **26** 1–15
[40] Panajotov K, Sciamanna M, Gatare I, Arteaga M and Thienpont H 2011 Nonlinear dynamics of vertical-cavity surface-emitting lasers *Adv. Opt. Technol.* **2011** 1–16
[41] Altés J B, Gatare I, Panajotov K, Thienpont H and Sciamanna M 2006 Mapping of the dynamics induced by orthogonal optical injection in vertical-cavity surface-emitting lasers *IEEE J. Quantum Electron.* **42** 198–207
[42] Toomey J P, Nichkawde C, Kane D M, Schires K, Henning I D, Hurtado A and Adams M J 2012 Stability of the nonlinear dynamics of an optically injected VCSEL *Opt. Express* **20** 10256
[43] Hurtado A, Schires K, Henning I D and Adams M J 2012 Investigation of vertical cavity surface emitting laser dynamics for neuromorphic photonic systems *Appl. Phys. Lett.* **100** 3–7
[44] Turconi M, Garbin B, Feyereisen M, Giudici M and Barland S 2013 Control of excitable pulses in an injection-locked semiconductor laser *Phys. Rev.* E **88** 022923
[45] Nahmias M A, Shastri B J, Tait A N and Prucnal P R 2013 A leaky integrate-and-fire laser neuron for ultrafast cognitive computing *IEEE J. Sel. Top. Quantum Electron.* **19** 1–12
[46] Hurtado A, Henning I D and Adams M J 2010 Optical neuron using polarisation switching in a 1550nm-VCSEL *Opt. Express* **18** 25170
[47] Hurtado A and Javaloyes J 2015 Controllable spiking patterns in long-wavelength vertical cavity surface emitting lasers for neuromorphic photonics systems *Appl. Phys. Lett.* **107** 241103
[48] Robertson J, Deng T, Javaloyes J and Hurtado A 2017 Controlled inhibition of spiking dynamics in VCSELs for neuromorphic photonics: theory and experiments *Opt. Lett.* **42** 1560
[49] Deng T, Robertson J, Wu Z M, Xia G Q, Lin X D, Tang X, Wang Z J and Hurtado A 2018 Stable propagation of inhibited spiking dynamics in vertical-cavity surface-emitting lasers for neuromorphic photonic networks *IEEE Access* **6** 67951–8
[50] Robertson J, Wade E, Kopp Y, Bueno J and Hurtado A 2020 Toward neuromorphic photonic networks of ultrafast spiking laser neurons *IEEE J. Sel. Top. Quantum Electron.* **26** 1–15
[51] Song Z W, Xiang S Y, Ren Z X, Wang S H, Wen A J and Hao Y 2020 Photonic spiking neural network based on excitable VCSELs-SA for sound azimuth detection *Opt. Express* **28** 1561
[52] Robertson J, Hejda M, Bueno J and Hurtado A 2020 Ultrafast optical integration and pattern classification for neuromorphic photonics based on spiking VCSEL neurons *Sci. Rep.* **10** 6098
[53] Song Z, Xiang S, Ren Z, Han G and Hao Y 2020 Spike sequence learning in a photonic spiking neural network consisting of VCSELs-SA with supervised training *IEEE J. Sel. Top. Quantum Electron.* **26** 1–9
[54] Panzeri S, Brunel N, Logothetis N K and Kayser C 2010 Sensory neural codes using multiplexed temporal scales *Trends Neurosci.* **33** 111–20
[55] Butts D A, Weng C, Jin J, Yeh C-I, Lesica N A, Alonso J-M and Stanley G B 2007 Temporal precision in the neural code and the timescales of natural vision *Nature* **449** 92–95
[56] Xiang S, Ren Z, Zhang Y, Guo X, Song Z, Wen A and Hao Y 2020. Hardware architecture and algorithm co-design for multi-layer photonic neuromorphic network with excitable VCSELs-SA. *Optical Fiber Communication Conf. (OFC) 2020* (Washington, DC: OSA) p W3A.1
[57] Gollisch T and Meister M 2008 Rapid neural coding in the retina with relative spike latencies *Science* **319** 1108–11
[58] Garbin B, Dolcemascolo A, Prati F, Javaloyes J, Tissoni G and Barland S 2017 Refractory period of an excitable semiconductor laser with optical injection *Phys. Rev.* E **95** 012214
[59] Zhang Z, Wu Z, Lu D, Xia G and Deng T 2020 *Nonlinear Dyn.* **99** 1103–14
[60] Izhikevich E M 2007 *Dynamical Systems in Neuroscience: The Geometry of Excitability and Bursting* (Cambridge, MA: MIT Press)
[61] Prescott S A, De Koninck Y and Sejnowski T J 2008 Biophysical basis for three distinct dynamical mechanisms of action potential initiation ed L.J. Graham *PLoS Comput. Biol.* **4** e1000198
[62] Izhikevich E M 1999 Class 1 neural excitability, conventional synapses, weakly connected networks, and mathematical foundations of pulse-coupled models *IEEE Trans. Neural Networks* **10** 499–507
[63] Sarantoglou G, Skontranis M and Mesaritakis C 2020 All optical integrate and fire neuromorphic node based on single section quantum dot laser *IEEE J. Sel. Top. Quantum Electron.* **26** 1–10
[64] Zhang Y, Xiang S, Guo X, Wen A and Hao Y 2018 Polarization-resolved and polarization- multiplexed spike encoding properties in photonic neuron based on VCSEL-SA *Sci. Rep.* **8** 16095
[65] Zhang Y, Xiang S, Gong J, Guo X, Wen A and Hao Y 2018 Spike encoding and storage properties in mutually coupled vertical-cavity surface-emitting lasers subject to optical pulse injection *Appl. Opt.* **57** 1731
[66] Robertson J, Wade E, Kopp Y, Bueno J and Hurtado A 2020 Toward neuromorphic photonic networks of ultrafast spiking laser neurons *IEEE J. Sel. Top. Quantum Electron.* **26** 1–15
[67] Deng T, Robertson J and Hurtado A 2017 Controlled propagation of spiking dynamics in vertical-cavity surface-emitting lasers: towards neuromorphic photonic networks *IEEE J. Sel. Top. Quantum Electron.* **23** 1–8
[68] Hodgkin A L and Huxley A F 1952 A quantitative description of membrane current and its application to conduction and excitation in nerve *J. Physiol.* **117** 500–44
[69] Prescott S A, De Koninck Y and Sejnowski T J 2008 Biophysical basis for three distinct dynamical mechanisms of action potential initiation *PLoS Comput. Biol.* **4** e1000198